PCCP

Accepted Manuscript

ROYAL SOCIETY OF CHEMISTRY

www.rsc.org/pccp

Physical Chemistry Chemical Physics

Full Paper

Reaction mechanism of PbS-on-ZnO heterostructure and enhanced photovoltaic diodes performance with interface modulated heterojunction energy band structure

Received 00th January 20xx,
Accepted 00th January 20xx

DOI: 10.1039/x0xx00000x

www.rsc.org/

Haili Li,[a] Shujie Jiao,[a,*] Jinxian Ren,[a] Hongtao Li,[a] Shiyong Gao,[a] Jinzhong Wang,[a] Dongbo Wang,[a] Qingjiang Yu,[a] Yong Zhang,[a] and Lin Li[b]

Room temperature successive ionic layer adsorption and reaction method is introduced for fabrication of Quantum Dots-on-Wide bandgap semiconductor. Detail explorations on how SILAR begins and proceeds are performed by analyzing the electronic structure variations of related elements at interfaces through X-ray photoelectric spectroscopy together with additional optical properties and X-ray diffraction characterizations. The distribution of PbS QDs on ZnO, which is actually critical for the optoelectrical applications of PbS stuff with large dielectric constant, shows close relationship with dipping orders. Successively distributed PbS QDs layer is achieved when the sample is immersed into Na_2S solution firstly. This is reasonable as the initial formation of different chemical bonds on ZnO nanorods are closely related with dangling bonds and defect states at surfaces. Most importantly, dipping order also influences their optoelectrical characteristics significantly, which can be well understood from the point of interface related heterojunction energy band structure. The formation mechanism of PbS QDs on ZnO is further proved by the fact that their device performances as photovoltaic diode are closely related with dipping orders. All these atomic understanding and explorations give emphasis on the fundamental role of surface chemistry on their structure and optoelectrical properties modulation and eventually device applications.

INTRODUCTION

Recent development of quantum confinement of nanomaterials has triggered a true revolution in high performance semiconductor materials and devices. Research attention on the regulation and application of the unique electrical, optical, magnetic and catalytic phenomena of quantum dots (QDs) that cannot be realized by their bulk counterparts has been growing at a quite rapid pace, especially for PbS QDs due to their notable size-based quantum properties arising from their large exciton Bohr radius (20 nm) and long exciton lifetime (200-800 ns).[1-5] Most importantly, it has been promised that even the Shockley-Queisser limit for solar cells (30%) can even be exceeded through multiple exciton effect (MEG) and promise in hot carrier extraction of QDs.[6-8] Formation and applications of pure PbS QDs are widely reported.[9-10] Meanwhile, suitable design and well-tuned fabrications of QDs-based heterostructures are urgently desired by the increasing demand of high performance and multi-functional application oriented heterostructures. Especially for QDs-on-Wide band gap semiconductor heterostructures due to the following three reasons: (I) Feasible achievement of broadened light absorption ranging from ultraviolet to visible and red, which provides advantages for applications in solar cells with high performance and low cost. (II) Improved carrier transport arising from suitable structure design, such as introduction of one dimensional ZnO nanorods. (III) Feasible fabrication procedures which can be easily achieved by simple and cost-effective methods, such as successive ionic layer adsorption and reaction (SILAR) method, etc. Until now, great achievements have been achieved in fabrications and applications of these heterostructures.[11-13] However there are still puzzles. The low quantum yield is one of them. To remedy this issue, both organic capping ligands and inorganic shells are introduced.[14.15] But new issues are brought for their device applications mainly due to the introduction of extra layer and Interfaces. As it is well-known that device performances of heterostructures are primly dominated by their interface related composition and structure. It is thus reasonable to believe that solving this problem by introducing an in-situ fabrication method may be a good idea. Two key points should be concerned for this case: (1) Efficient electron transport from PbS QDs directly to oxide semiconductor, which is very sensitive to the surface/interface related composition and defects.[9] (2) Separation distance tuning between PbS QDs, which influences the carrier transport within QDs layer. Consequently, understanding the adsorption and bonding properties of ions on the surface of ZnO and growth process of SILAR method is of great

[a] School of Materials Science and Engineering, Harbin Institute of Technology, Harbin 150001, P. R. China
[b] Key laboratory for Photonic and Electronic Bandgap Materials, Ministry of Education, Harbin Normal University, Harbin, 150025, P. R. China
Corresponding author: shujiejiao@gmail.com

significance for controllable growth of materials with selected structures and physic-chemical properties. Kamat et al explored the growth process of CdSe by X-ray absorption near edge structure (XANES).[16] Their research confirmed that SILAR is a simple and effective mean to deposit semiconductor with intimate interfacial contact by observing the interfacial charge depression tuned by deposition steps.[16] But, both deeper explorations and physical analysis on tunable growth and carrier transport mechanisms of this heterostructure are needed by their potential device applications such as band broadening photodetector and solar cell, etc.

Herein, PbS QDs are formed on ZnO nanorods by room temperature SILAR method and the atomic tracking on the beginning and formation process of this heterostructure is achieved by X-ray photoelectron spectroscopy characterization. Effects of dipping order on their optoelectrical properties of ZnO/PbS heterostructure are analyzed from the point of interface related energy band modulations.

EXPERIMENTAL SECTION

Preparation of different ZnO nanostructures

ZnO nanomaterials mentioned in this report were formed by hydrothermal method as mentioned in our precious work.[17,18] In briefly, ZnO seed layers were firstly formed on ITO or quartz substrate by sol-gel based dip coating method and ZnO nanorods were formed on substrates in nutrient solution consisting of zinc acetate dehydrate ($Zn(AC)_2{\cdot}2H_2O$) (0.03 M) and HMT (0.03 M) at 90 ^oC for 4h. Only ZnO nanomaterials mentioned in Figure 3(b) are formed by using $ZnCl_2$ as zinc source instead of $Zn(AC)_2{\cdot}2H_2O$.[18]

Pb^{2+} or S^{2-} incorporated ZnO by SILAR method

Na_2S (0.02 M) and $Pb(NO_3)_2$ (0.05 M) solutions are formed in co-solvent with ethanol/water (2:1/v:v) and ethanol/water (1:1/v:v), respectively. For Pb^{2+} incorporated ZnO (Pb-ZnO), optimized ZnO sample was immersed into $Pb(NO_3)_2$ solution for 30 s and rinsed by pure ethanol. Similarly, S^{2-} incorporated ZnO (S-ZnO) was formed by immersing ZnO sample into Na_2S solution for 60 s and rinsed by pure ethanol. Both the Pb-ZnO and S-ZnO samples used for XPS characterization are formed by repeating the corresponding dipping and rinsing processes 6 times.

Formation of PbS QDs on ZnO by SILAR method

To form PbS QDs on ZnO, the optimized ZnO sample was successively immersed into two different solutions for 30 s and 60 s each. After each immersion, the films were rinsed with pure ethanol to remove excess precursors and blow to dry at room temperature before next dipping.[19] The samples are formed by repeating these immersion cycles for 4 times. The sample began with immersion into $Pb(NO_3)_2$ firstly is designated as "Pb-S-ZnO".[19] "S-Pb-ZnO" sample is formed by being dipped into Na_2S solution firstly.

Fabrication of PbS QDs-based Photovoltaic diodes

The QDs-modified ZnO electrode and a copper counter electrode were sandwiched using 60 mm thick sealing material. Water/methanol (5:5 by volume) solution was used as a co-solvent of the polysulfide electrolyte. The electrolyte solution consists of Na_2S (0.5 M), S (0.125 M), and KCl (0.2 M). The active area of the cell was 0.3 cm^2.

Characterization

Scanning electron microscope (SEM, KYKY-EM6000C, 15 KV) and X-ray diffractometer (XRD, Philips-FEI, Netherlands, Cu Ka radiation) were used for structure characterization. Their composition and bond banding properties were achieved by Bruker's Energy Disperse Spectroscopy (EDS, 15 kV, HORIBA Jobin Yvon) and X-ray photoelectric spectroscopy (XPS, Al Kα, PHI 5700 ESCA System, Physical Electronics, USA). Their optical properties and electrical properties were performed by Ultraviolet-visible Spectra (UV 1700-1800, Fenghuang, Shanghai). I-V characterizations of the as-synthesized devices are measured by the electrochemical workstation (Corrtest, CS350) with a three electrodes system. The solar light is simulated by xenon lamp (1.5 AM, 100 mW/cm^2).

RESULTS AND DISCUSSION

How SILAR Begins

For a better understanding on the formation of PbS QDs on ZnO heterostructure by SILAR method and eventually structure control and performance modulations, one primarily important issue is firstly explored, that is, how SILAR begins. To better solve this issue at atomic level, XPS investigation is introduced as it only detects surface information and very sensitive to electronic and chemical state of elements that exist within a material and elemental composition in the parts per thousand ranges. The XPS wide survey spectra of pure ZnO, S-ZnO and Pb-ZnO are given in Figure 1. The peaks marked by dash black lines in Figure 1 belong to Zn and O elements. Pb and S peaks are obtained besides Zn, O and C peaks for Pb-ZnO and S-ZnO samples, separately. Their corresponding atomic concentrations ratios are exhibited in Table 1. It is obvious that the atom ratio of Zn and O increased slightly from 1:1.81 for pure ZnO to 1:1.67 for S-ZnO and decreased significantly to 1:5.95 for Pb-ZnO. These obvious variations indicate the significant effects of ions incorporations on their bonding properties. The substantial decline in the Zn/O atom ratio of Pb-ZnO may be an indication of the substitution of Pb for Zn. Taking the similarity of O and S into consideration, the slight decrease in the Zn/O atom ratio for S-ZnO sample may illustrate that the incorporation of S^{2-} may have close relationship with oxygen-related defects. To further confirm these deductions, detail analysis are performed as follows:

Incorporation of Pb^{2+} on the surface of ZnO

Figure 2 shows the XPS spectra of O 1s core-level of pure ZnO and Pb-ZnO. Three Gaussians fitting peaks marked as (1)-(3) were used to fit the experimental data for pure ZnO in Figure 2a.[20-21] The low binding energy peak (1), positioned at –529.7 eV, is commonly assigned to O^{2-} ions in the Zn–O bonding of the wurtzite structure of ZnO. The middle binding energy peak (2) located at 530.3 eV should belong to the O^{2-} in the oxygen deficiency regions. The high binding energy peak (3) locates at 531.6 eV, which can be attributed to the related OH groups

absorbed on the surface of the ZnO nanorods. Similarly, the O 1s region of Pb-ZnO is also be fitted by Gaussians peaks as shown in Figure 2b. The Gaussians peaks (0) and (4) located at 529.1 eV and 532.2 eV are obtained besides O1s peaks of ZnO mentioned in Figure 2a. The Gaussians peak (0) can be attributed to the formation of Pb-O bonds.[22] The Gaussians peak (4) may be arising from the residual acetate or nitrate[23] or chemisorbed oxygen. The formation of Pb-O bonds indicates the incorporation of Pb^{2+} into ZnO. Meanwhile, the substitution of Pb element for Zn element can be confirmed by the absence of peak (1) related to the O^{2-} ions in the wurtzite structure of the hexagonal Zn^{2+} ion array. The oxidation of Pb element is analyzed by Pb 4f spectrum in Figure 2c. Both Pb $4f_{5/2}$ and Pb $4f_{7/2}$ peaks are obtained with spin–orbital splitting value of 4.9 eV corresponding to lead oxide. The Pb $4f_{7/2}$ peak locates at 138.2 eV belongs to Pb_4O_3.[24,25] The absence of Pb $4f_{7/2}$ at 136.6 eV demonstrates that the incorporated Pb in the ZnO is in the mixed valence states not metal Pb.[26] The substitution of Pb for Zn is reasonable based on the fact that the ionic radii of Pb^{2+} (0.119 nm) is larger than Zn^{2+} (0.074 nm). This substitution is further proved by the complementary of Pb element and Zn element in the EDS in Figure 2d.

Incorporation of S^{2-} on the surface of ZnO

Figure 3a is the XPS spectra of O 1s of S-ZnO. Three fitting Gaussians peaks marked as (1)-(3) were used to fit the experimental data as mentioned for pure ZnO. The intensity ratio of O^{2-} in the oxygen deficiency regions and the related OH group absorbed on the surface of the ZnO decreased obviously. This result indicates that S^{2-} ions mainly incorporate with the oxygen vacancies and OH groups on the surface of ZnO. To further confirm the incorporation of S^{2-} ions with the oxygen vacancies, ZnO nanomaterials with high density of oxygen defects are formed by using $ZnCl_2$ as zinc source.[17,18] According to our precious reports, optical property of nanomaterials is closely related with their nature bandgap and trapping states as well.[17,18] For pure ZnO synthesized by $ZnCl_2$, obvious oxygen defects related absorption at 550 nm is observed besides the typical absorption peak of ZnO at 380 nm as shown in Figure 3b. By immersing the substrate into Na_2S solution for three times, the absorption ratio of visible light to ultraviolet (UV) light decreased significantly due to the occupation of oxygen vacancy by S^{2-}. This is reasonable as the similarity of S atom to O atom, which provides it with better adaptability to fix oxygen relate defects, especially for vacancy. This can be further confirmed by the formation of Zn-S bonds observed in their Zn 2p spectrum in Figure 2c. Two strong peaks positioned at 1021.18 eV and 1044.28 eV are observed for pure ZnO, which are in good accordance with the reported binding energies of Zn $2p_{3/2}$ and Zn $2p_{1/2}$ in ZnO.[27] Its spin–orbital splitting value of 23.1 eV confirms that Zn is presented as Zn^{2+}. For S-ZnO, the movement of Zn 2p peaks to higher values indicates the formation of Zn-S bonds.[28]

Formation of PbS by SILAR method

Figure 4a shows the XRD spectra of Pb-S-ZnO and S-Pb-ZnO annealed in argon atmosphere at 180 ^{o}C for 30 min. It is obvious that typical ZnO peaks (JCPDS No. 1451) are observed for both samples.[29] Besides ZnO peaks, the observed diffraction peaks of S-Pb-ZnO is in good accordance with the (200), (220), (311), (222) reflections of PbS in its cubic phase (JCPDS Card File No. 05-0592).[30] No other impurities are observed indicating the formation of pure PbS on ZnO. While for Pb-S-ZnO sample, only two PbS diffraction peaks with much lower intensity are detected. To further confirm the formation of PbS on ZnO for Pb-S-ZnO sample, XPS characterization is given in Figure 4b-4d. Figure 4b is the XPS wide survey spectra of Pb-S-ZnO. It is obvious that both Pb and S elements are observed besides Zn, O and C. The XPS spectra of S 2p and Pb 4f of Pb-S-ZnO heterostructure are given in Figure 4c and 4d. The shift of S peaks to lower binding energy confirms the formation of large amount of Pb-S bonds instead of Zn-S bonds.[31] Besides, the formation of $PbSO_3$ or $PbSO_4$ is also eliminated based on the fact that no obvious XPS peaks at around 166 eV or 169 eV are observed.[32] The formation of PbS can be further confirmed by the peak shift of Pb peak of Pb-S-ZnO to lower binding energy compared to Pb-ZnO.[33]

Detail information on the morphology and distribution of PbS QDs on ZnO is exhibited in Figure 5. The as-synthesized ZnO nanorods are not uniform with a diameter distribution from 20 nm to 110 nm. The average diameter of ZnO nanorods in Figure 5a is about 50 nm. Obvious QDs are observed on the surface of ZnO for Pb-S-ZnO in Figure 5b, but no obvious diameter variation is observed for ZnO nanorods before and after SILAR process. While for S-Pb-ZnO in Figure 5c, densely distributed QDs are formed. This is in good accordance with the much higher visible light absorption of S-Pb-ZnO in Figure 5d as light absorption of solid state materials is generally proportional to thickness.[19] The immersion time dependence light absorption spectra of Pb-S-ZnO and S-Pb-ZnO are given in the supporting information S1, in which light absorption increases with cycle times.[16] These results further confirm that increase in the visible light absorption for S-Pb-ZnO is an indication of the formation of higher amount of PbS QDs on ZnO. The different distribution of QDs on ZnO caused by variations in dipping orders is further confirmed by samples formed with more dipping times. Their SEM images are illustrated in Figure 5e and 5f. These samples in Figure 5e and 5f are formed by dipping ZnO into $Pb(NO_3)_2$ or Na_2S solution 3 times before being dipped into the other solution as mentioned in our precious work.[19] The sample was finally formed by repeating the dipping and rinsing cycle for 4 times.

Based on the above analysis, the beginning and growth process of PbS QDs on ZnO can be described at nanoscale as follows: ZnO nanorods were firstly formed on the substrate by hydrothermal method. ZnO is commonly a n type semiconductor due to the existence of oxygen vacancy or zinc interstitial, etc.[34] Together with the existence of surface dangling bond, the schematic diagram for ZnO nanorods is exhibited in Figure 6a. By immersing ZnO nanorods into $Pb(NO_3)_2$ solution, Pb^{2+} ions are absorbed onto ZnO by forming Pb-O bonds. After being washed by ethanol, some loosely attached Pb^{2+} ions are washed away leaving Pb^{2+} ions closely bonded on the surface of ZnO. In this case, Pb mainly exists in

its oxide by forming Pb-O bonds as shown in Figure 6b. Thanks to the fact that formation of PbS is thermodynamically easier and PbS is feasibly formed through the reaction between Pb^{2+} and S^{2-} during the immersion of substrate into Na_2S solution as shown in Figure 6c. As for S-Pb-ZnO sample, Zn-S bonds are firstly formed due to the low solubility product constant (K_{sp}) compared to $Zn(OH)_2$.[35] PbS is then formed by reacting with Pb^{2+} as shown in Figure 6e. The full coverage of ZnS and eventually PbS on ZnO may arise from the abundant existence of oxygen-related defects and dangling -OH bonds on the surface of ZnO which facilitates the incorporation of S^{2-} ions on the surface of ZnO for S-Pb-ZnO as illustrated by the thin purple layer in Figure 6e.

Surface chemistry tuned optoelectrical properties of PbS QDs-on-ZnO heterostructures

Besides the effect of dipping order on the distribution of QDs on ZnO, the formation of Zn-S or Pb-O bonds at interfaces also influences their optoelectrical properties significantly. Figure 7a and 7b are I-V curves of Pb-S-ZnO and S-Pb-ZnO heterostructures and insets are their graphic representations. ZnO nanomaterials mentioned in this part are formed on quartz substrate and ohmic contacts are achieved by forming indium electrodes on ZnO and PbS-ZnO as mentioned before.[19] The I-V curves of Pb-S-ZnO heterostructure in Figure 7a measured under different light illumination shows similar characteristics indicating its wavelength-independent electrical transport characteristic. Thus, the photo-induced carrier generation and transport can be explained by the same model: Ideal reverse current in negative voltage section is obtained by giving nearly constant reverse saturation current at high negative bias. At lower negative voltage, the reverse current is not as low as the theoretical prediction. We assume this high reverse current to defect-assisted tunnelling and field-dependent tunnelling via defects located in the space-charge region, which is in good accordance with S. Tüzemen's report.[36] Generally, the I-V behaviour can be represented by Equation 1:[37]

$$I = I_0 \exp(qV / nkT) \quad (1)$$

Where *V* is the applied voltage and the ideality factor n can be calculated by curve fitting. The unrealistic ideality factor calculated here for Pb-S-ZnO indicates that tunnelling current domains the carrier transport within this heterostructure.[39] The corresponding equilibrium band diagram is illustrated in the inset of Figure 7a. The different band bending at interface compared to ideal situation can be attributed to the existence of defects in the diodes.The Fermi level keeps constant across the entire region of the heterojunction owing to the diffusion of carriers' with forming the depletion regions and built-in electric field. The band diagrams under different voltage is given in the Supporting Information S2, which show similar regulation as the work reported by Y. Guo, et al.[38] Under the forward bias, majority carriers transport domains the current variations, which increases along with voltage. But, it increases slowly compared to ideal situation. This difference can be attributed to the formation of insulating layer which leads to the formation of weak inversion layer at higher voltage. As for S-Pb-ZnO, totally different I-V curves are obtained as shown in Figure 7b. The I-V curves measured under different light illuminations show different characteristics. For I-V curves measured under dark and green light, the current increases slowly at positive voltage while higher current increase rate is obtained at reverse voltage. When the sample is illuminated by ultraviolet light, much higher photocurrent is obtained at both forward and reverse voltages. All these variations can be explained by the formation of ZnS at the interface between PbS and ZnO and understood in terms of the equilibrium band alignment as illustrated in the inset of Figure 7b.[40] Figure 7c and 7d are band diagram under positive and negative bias. Possible sources of the deep level traps in this S-Pb-ZnO sample responsible for the observed carrier tunnelling include oxygen impurities, crystal defects caused by the substitution of Pb for Zn and structural defects arising from the interfaces between QDs and ZnO. Under green light illumination, photo-induced electrons and holes are mainly generated in PbS. Holes and electrons are expected to be extracted by negative and positive electrodes, respectively. Unfortunately, some photo induced electrons also transport from PbS to ZnS due to its lower band position as shown by the schematic diagram in Figure 7c. Thus, some holes are combined with electrons at the interface between PbS and ZnS, which well explains the low current at positive voltage. Increasing voltage may facilitates the transport of holes from ZnS to ZnO, but not much owing to its much higher valance band position. While under reverse voltage, the conduction band offset of ZnO and ZnS is decreased while the conduction band offset of ZnS and PbS is increased, which promote the transport of electrons from PbS to ZnO through ZnS layer and eventually collected by positive electrode. At the same time, holes are extracted by negative electrode directly as shown by the schematic diagram in Figure 7d. In other words, the separation efficiency of photo-induced carriers is improved in contrast with the situation at positive voltage, which results in obvious increases in current with reverse voltage compared to the case with forward voltage. At the same time, the I-V curve measured under ultraviolet light can also be understood: When this heterostructure is illuminated by ultraviolet photons with energy corresponding to the band gap of ZnO, most of photo-induced carriers are produced within ZnO and possess a much higher concentration than photo-induced carriers generated in PbS under green light illumination due to the much thinner PbS layer. Based on the band diagram analysis in Figure 7c-7d, it is clear that both electrons extraction from ZnO to positive electrode and holes transport from ZnO to PbS are feasible when positive voltage is applied on ZnO, which well explains the much higher current in this case. When a negative voltage is applied on ZnO, the conduction band offset of ZnO and ZnS is increased, which may hinder electron transport from ZnO to ZnS. But, the generation of large amount of photo-induced electrons may facilitate the tunnelling process of photo-generated carriers. Besides, the barrier height for electron transport under negative voltage is much lower than that for hole transport at positive voltage. Thus, the much higher current for ultraviolet light illuminated S-Pb-ZnO is understandable.

Based on the above analysis, it is reasonable to believe that both the structure and the optoelectrical properties of PbS-on-ZnO heterostructures are closely related with dipping orders and one can suit their dipping orders to their local conditions. Besides, the successive distribution of PbS QDs on ZnO may decrease the transport barrier for photo-induced carriers within PbS, which might provide another way for improvement of carrier transport besides ligands exchange method and partly eliminate the negative effects of its large dielectric constant on device applications. This is confirmed by their photovoltaic diode applications. Figure 8a and 8b are their J-V curves of open solar cells measured under the dark and AM 1.5 condition. The open solar cells are formed by using Pb-S-ZnO/ITO and S-Pb-ZnO/ITO as anode electrodes, respectively. Obvious current increases are obtained in both cases under AM 1.5. Almost no obvious open voltage is obtained under AM 1.5 for Pb-S-ZnO based solar cell. While about 5 times higher open voltage is obtained for S-Pb-ZnO based photovoltaic diode compared to the Pb-S-ZnO based photovoltaic diode. The successive distribution of QDs on the surface of ZnO shall be one of the essential reasons for the high performance S-Pb-ZnO sample. Meanwhile, the depression of sulphur deficiencies and surface states on the surface of S-Pb-ZnO sample caused by the final adsorption of Pb^{2+} on the surface may further contribute to its high device performance. This is in good accordance with the conclusion mentioned in Minqiang Wang and M. Law's reports that the absence of abundant sulphur deficiencies and surface states contribute to the solar cell performance improvement.[41,42] Figure 8c and 8d are the time-dependent photoresponse spectra of Pb-S-ZnO and S-Pb-Zn based solar cells. Much higher on-off voltage variation is obtained for S-Pb-ZnO in Figure 8d, which are in good accordance with the result in Figure 8a and 8b. These results may provide another idea on the improvements of QDs-on-wide bandgap semiconductor based photovoltaic devices. Besides, the efficiency of photovoltaic diodes mentioned in this article can be improved by forming sealed cells and introducing blocking layers. More exploration on this issue will be discussed in future.

CONCLUSION

PbS QDs are successfully formed on ZnO nanorods by SILAR method at room temperature. The growth mechanism is explored at atomic scale by XPS characterization together with optical properties and element distribution analysises. Analyzed from the point of view of electronic structure variations and related elemental compositions properties, the beginning and growing process can be concluded as follows: For Pb-S-ZnO sample, the formation of PbS QDs on ZnO begins with the formation of Pb-O bonds through substitution of Pb for Zn. While for S-Pb-ZnO Zn-S bonds are firstly formed. PbS QDs are finally fabricated on the surface of ZnO owing to thermodynamically supported formation of Pb-S bonds. Both the distribution and optoelectrical properties of the as-synthesized heterostructures show close relationship with dipping orders. I-V curves of S-Pb-ZnO measured under different light illuminations show different characteristics owing to the formation of ZnS thin film between ZnO and PbS. Obvious different device performances are obtained for Pb-S-ZnO and S-Pb-ZnO based photovoltaic diodes, which further confirm the significant role of interface characteristics within heterostructures on their high performance device applications.

ACKNOWLEDGMENT

This work is supported by National Natural Science Foundation of China (Grant No. 61306014 and 61574051)

REFERENCES

(1) R. P. G.McNeil; M. Kataoka; C. J. B. Ford; C. H. W. Barnes; D. Anderson; G. A. C. Jones; I. Farrer and D. A. Ritchie, *Nature,* 2011, **477**, 439.
(2) I. Moreels; K. Lambert; D. Smeets; D. D. Muynck; T. Nollet; J. C. Martins; F. Vanhaecke; A. Vantomme; C. Delerue; G. Allan and Z. Hens, *Nano,* 2009, **3**, 3023-3030.
(3) F. Todescato; A. S. R. Chesman; A. Martucci; R. Signorini and J. J. Jasieniak, *Chem. Mater.,* 2012, **24**, 2117–2126.
(4) X. L. Dai; Z. X. Zhang; Y. Z. Jin, Y. Niu; H. J. Cao; X. Y. Liang, L. W. Chen; J. P. Wang and X. P. Peng, *Nature*, 2014, **515**, 96.
(5) B. H. Kim; M. J. Hackett; J. Park and T. Hyeon, *Chem. Mater.,* 2014, **26**, 59.
(6) G. Konstantatos and E. H. Sargent, *Appl. Phys. Lett.* 2007, **91**, 173505.
(7) S-C Lin; Y-H Lee; C-H Chang; Y-J Shen and Y-M Yang, *Appl. Phys. Lett.,* 2007, **90**, 143517.
(8) Y-L Lee and Y-S Lo, *Adv. Funct. Mater.,* 2009, **19**, 604.
(9) X. Cao; C. M. Li; H. Bao; Q. Bao and H. Dong, *Chem. Mater.* , 2007, **19**, 3773.
(10) F. C. J. M. Veggel, *Chem. Mater*. 2014, **26**, 111.
(11) Z. H. Sun; Z. K. Liu; J. H. Li; G-A Tai; S-H Lau; F Yan, *Adv. Mater.*, 2012, **24**, 5878.
(12) K. Szendrei; F. Cordella; M. V. Kovalenko; M. BÖberl; G. Hesser; M. Yarema; D. Jarzab; O. V. Mikhnenko; A. Gocalinska; M. Saba; F. Quochi, et al, *Adv. Mater.,* 2009, **21**, 683.
(13) Q. Kang; S. H. Liu; L. X. Yang; Q. Y. Cai; C. A Grimes, *Appl. Mater. Interfaces*, 2011, **3**, 746.
(14) A. J. Morris-Cohen; M. Malicki; M. D. Peterson; J. W. J. Slavin; E. A. Weiss, *Chem. Mater.*, 2013, **25**, 1155.
(15) S. KrÜger; S. G. Hickey; S. Tscharntke; A. EychmÜller, *J. Phys. Chem. C*, 2011, **115**, 13047.
(16) M. A. Becker; J. G. Radich; B. A. Bunker; P. V. Kamat, *J. Phys. Chem. Lett.*, 2014, **5**, 1575.
(17) H. L. Li; S. J. Jiao; S. S. Bai; H. T. Li; S. Y. Gao; J. Z. Wang; Q. J. Yu; F. Y. Guo; L. C. Zhao, *Phys. Stat. Sol. A*, 2014, **211**, 595.
(18) H. L. Li; S. H. Jiao; H. T. Li; L. Li, *J Mater. Sci: Mater. Electron.*, 2014, **25**, 2569.
(19) H. L. Li; S. H. Jiao; S. Y. Gao; H. T. Li; L. Li; X. T. Zhang, *CrystEngComm*, 2015, **17**, 4722.
(20) J. Das; S. K. Pradhan; D.R. Sahu; D. K. Mishra; S. N. Sarangi; B. B. Nayak; S. Verma; B. K. Roul, *Physica B*, 2010, **405**, 2492.
(21) H. Zhou; Z. Li, *Mater. Chem. and Phys.*, 2005, **89**, 326.

(22) J. M. Baker; R. W. Johnson; R. A. Pollak, *J. Vac. Sci. Technol.*, 1979, **16**, 1534.
(23) V. K. Kaushik, *J. Electron. Spectrosc. Relat. Phenom.*, 1991, **56**, 173,
(24) S. Ameen; M. S. Akhtar; H-K Seo; S. K. Young; S. S. Hyung, *Chem. Eng. J.*, 2012, **187**, 351.
(25) M. M. Rahmana; K. M. Krishna; T. Soga; T. Jimbo; M. Umeno, *J. Phys. Chem. Solids*, 1999, **60**, 201.
(26) N. Kannadasan; N. Shanmugam; K. Sathishkumar; S. Cholan; R. Ponnguzhali; G. Viruthagiri, *Spectrochimica Acta Part A: Molecular and Biomolecular Spectroscopy*, 2015, **143**, 179.
(27) R. Gaashani; S. Radiman; A. R. Daud; N. Tabet, Y. Al-Douri, *Ceram. Int.*, 2013, **39**, 2283.
(28) F. J. Wang; J. Liu; Z. J. Wang; A-J Liu; H. Luo; X. B. Yu, *J. Electrochem. Soc.*, 2011, **158**, H30.
(29) M-K Liang; M.J. Limo;, A. Sola-Rabada; M. J. Roe; C. C. Perry, *Chem. Mater.,* 2014, **26**, 4119.
(30) L. F. Koao; F. B. Dejene; H. C. Swart, *Int. J. Electrochem. Sci.*, 2014, **9**, 1747.
(31) J. Liu; H. Yu; Z. Wu; W. Wang; J. Peng; Y. Cao, *Nanotechnology*, 2008, **19**, 345602.
(32) N. Zhao; T. P. Osedach; L-P Chang; S. M. Geyer; D. Wanger; M. T. Binda; A. C. Arango; M. G. Bawendi; V. Bulovic, *ACS Nano.*, 2010, **4**, 3743.
(33) C. D. Wagner; W. M. Riggs; L. E. Davis; J. F. Moulder. Handbook of X-Ray Photoelectron Spectroscopy. Muilenberg. G. E.; VCH: U.S.A., 1979; Vol. 2, pp 150–151.
(34) D-H Kim; G-W Lee; Y-C Kim. *Solid State Commun.,* 2012, **152**, 1711.
(35)J. Xu; Z. H. Chen; J. A. Zapien; C-S Lee, W. J. Zhang, *Adv. Mater.,* 2014, 26, 5337; E. Edri; E. Rabinovich; O. Niitsoo; H. Cohen; T. Bendikov; G. Hodes. *J. Phys. Chem. C.*, 2010, **114**, 13093.
(36) E. Gür; S. TÜzemen; B. Kiliç; C. Coşkun, *J. Phys.: Condens. Matter.*, 2007, **19**, 196206.
(37) X. A. Cao; E. B. Stokes; P. M. Sandvik; S. F. LeBoeuf; J. Kretchmer; D. Walker, *Electr. Device L.*, 2002, **23**, 9.
(38) T. C. Zhang; Y. Guo; Z. X. Mei; C. Z. Gu; X. L. Du, *Appl. Phys. Lett.*, 2009, **94**, 113508.
(39) D. J. Dumin; G. L. Pearson, *J. Appl. Phys.*, 1965, **36**, 3418.
(40) M. Sookhakian; Y. M. Amin; W.J. Basirun; M.T. Tajabadi; N. Kamarulzaman, *J. Lumin.*, 2014, **145**, 244.
(41) Z. Yang; M. Wang; S. Shukla; Y. Zhu; J. Deng; H. Ge; X. Wang; Q. Xiong, *Sci. Rep.*, 2015, **5**, 11377.
(42) M. Limpinsel; N. Farhi; N. Berry; J. Lindemuth; C. L. Perkins; Q. Lin; M. Law, *Energy. Environ. Sci.*, 2014, **7**, 1974.

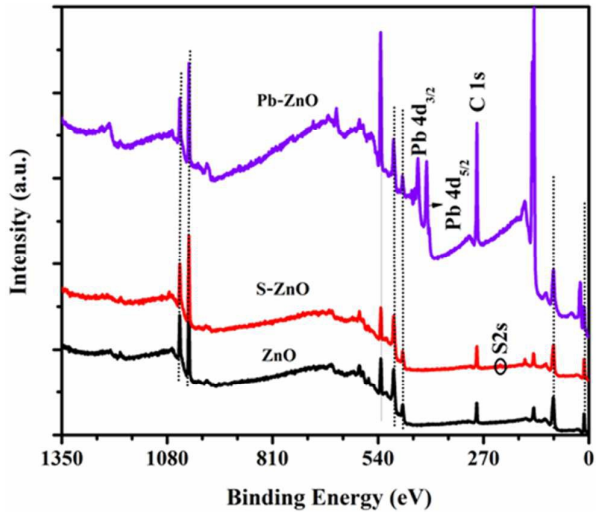

Figure 1 XPS wide survey spectra of ZnO, S-ZnO and Pb-ZnO.

Table 1 Atomic concentration ratios of elements on the surface of ZnO, S-ZnO and Pb-ZnO measured by XPS characterization.

Element	Zn (%)	O (%)	Pb (%)	S (%)	C (%)
ZnO	18.43	33.45	0	0	48.12
S-ZnO	18.54	30.91	0	4.73	45.83
Pb-ZnO	4.98	29.65	4.98	0	50.27

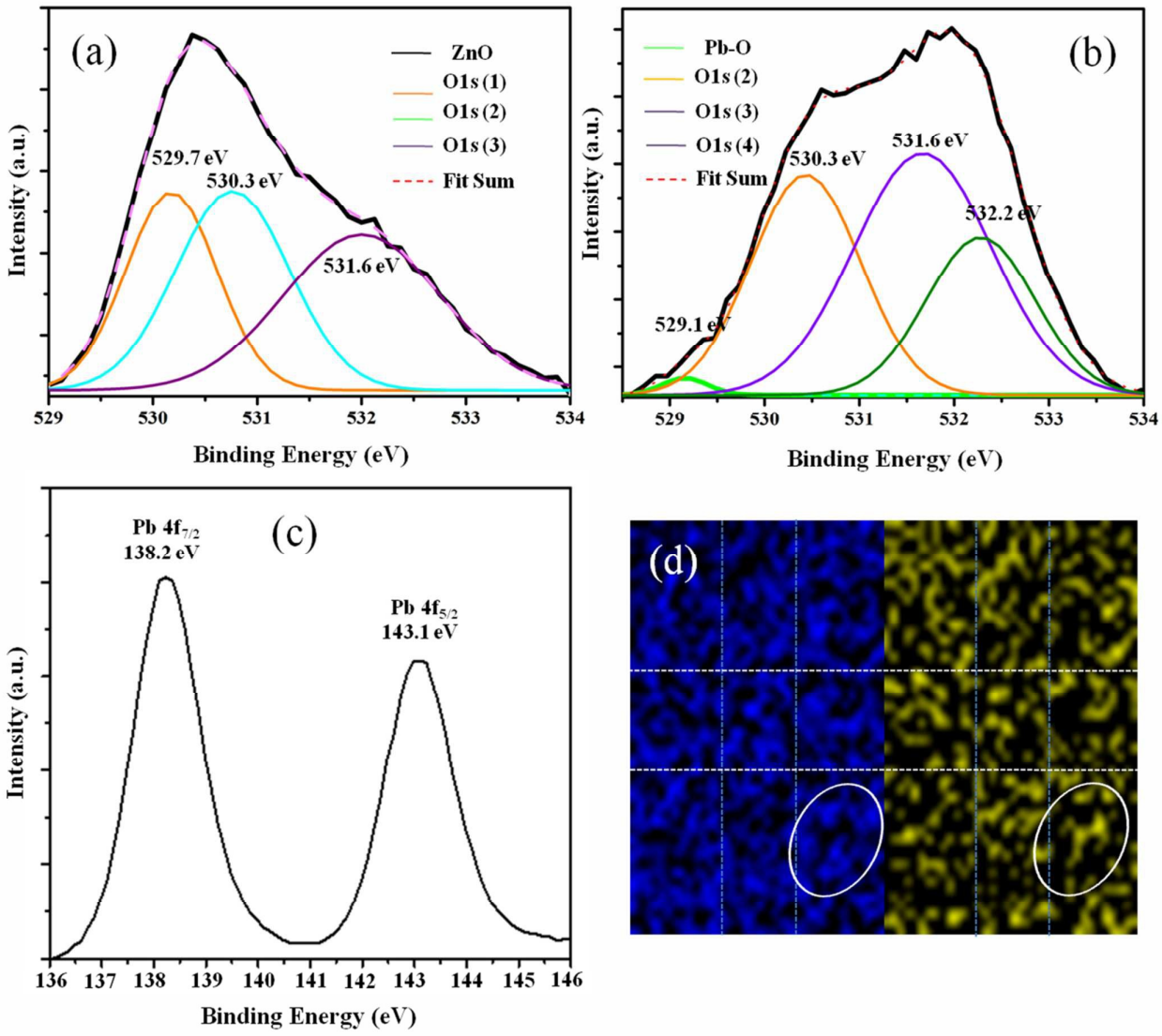

Figure 2 (a) and (b) XPS spectrum and peak fitting curves of O 1s for ZnO and Pb-ZnO. (c) XPS spectrum of Pb 4f for Pb-ZnO. (d) EDS spectrum of Zn element (blue) and Pb element (yellow).

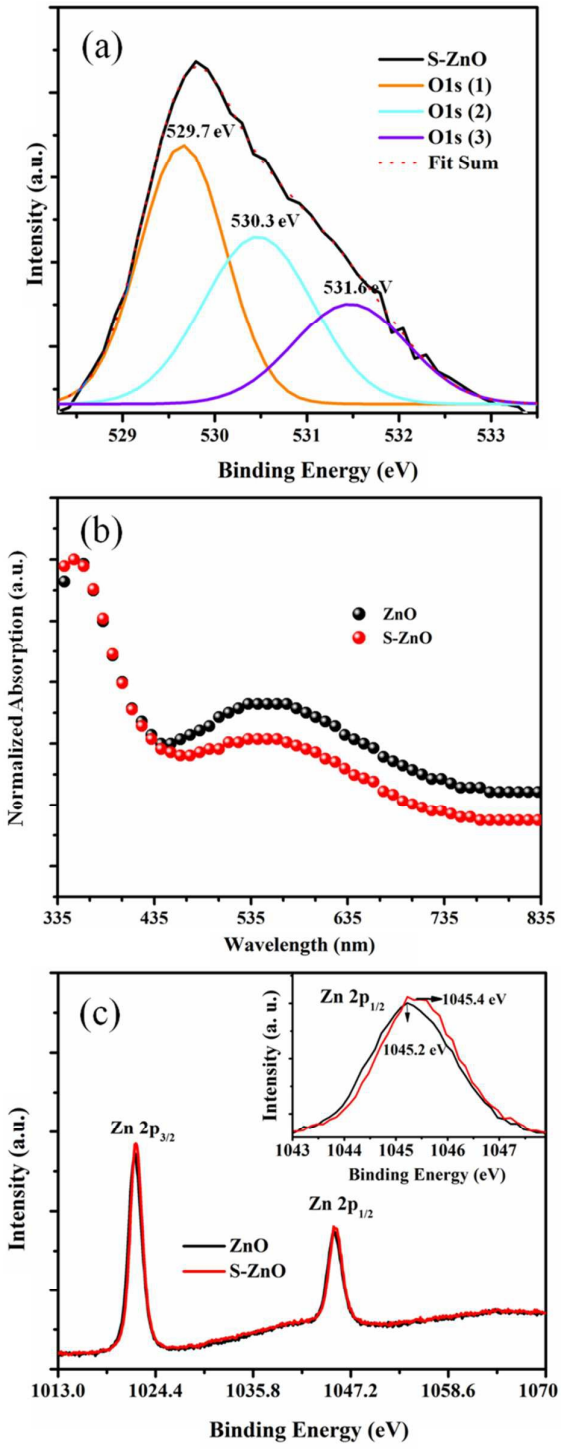

Figure 3 (a) XPS spectrum and peak fitting curves of O 1s core-level of pure ZnO. (b) Light absorption of ZnO and S-ZnO. (c) XPS spectra of Zn 2p for S-ZnO. ZnO used in Figure 3(b) is synthesised by using $ZnCl_2$ as zinc source.

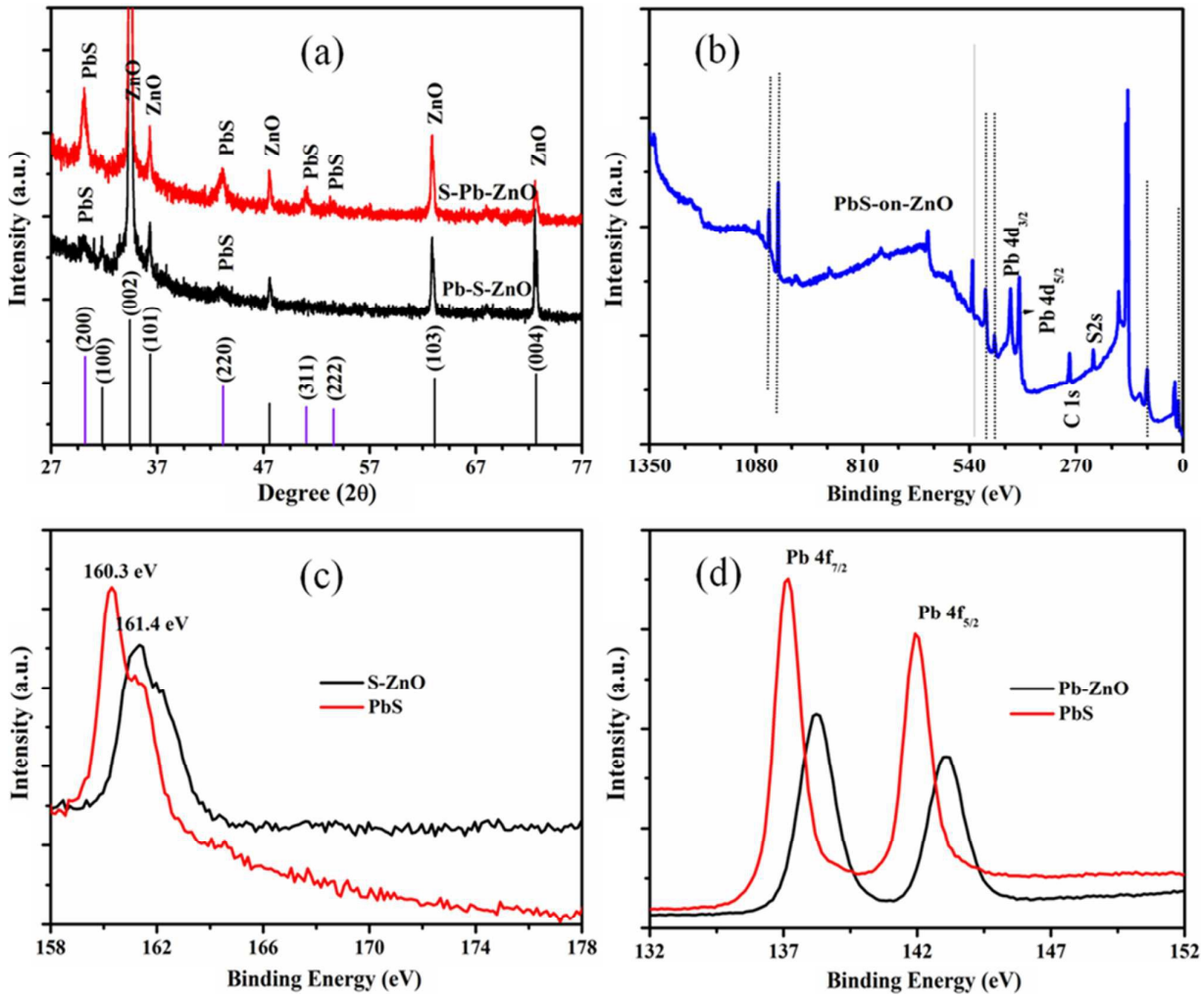

Figure 4 (a) XRD spectra of Pb-S-ZnO and S-Pb-ZnO annealed in argon at 180 ^{o}C for 30 min. (b) XPS wide survey spectrum of Pb-S-ZnO. (C) and (d) The XPS spectra of S 2p and Pb 4f for Pb-S-ZnO sample.

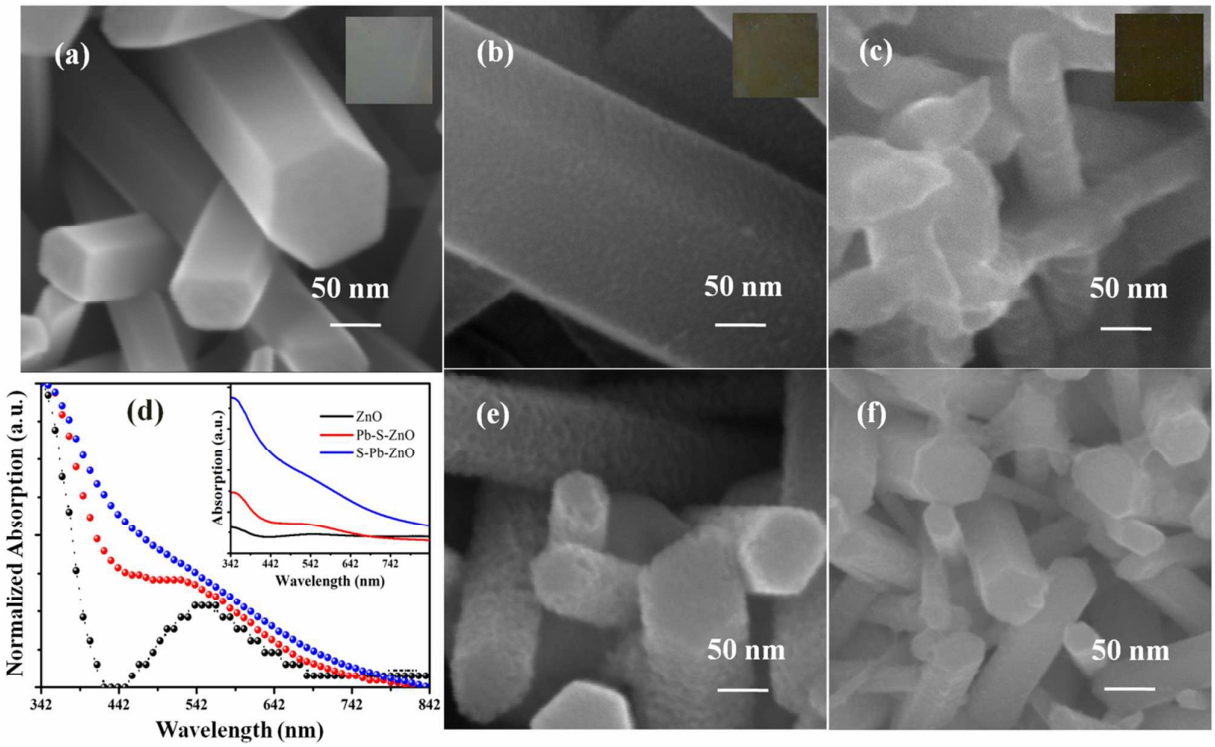

Figure 5 (a)-(d) SEM and normalized light absorption spectra of pure ZnO, Pb-S-ZnO and S-Pb-ZnO. Insets of Figure 5(a)-5(c) are their corresponding optical photographs. Inset of Figure 5(d) shows light absorption spectra of pure ZnO, Pb-S-ZnO and S-Pb-ZnO. (e) SEM image of PbS-on-ZnO formed by repeating the following procedures three times: Dipping in $Pb(NO_3)_2$ solution for three times and then in Na_2S solution for one time. (f) SEM image of PbS-on-ZnO formed by repeating the following procedures three times: Dipping in Na_2S solution for three times and then in $Pb(NO_3)_2$ solution for one time.

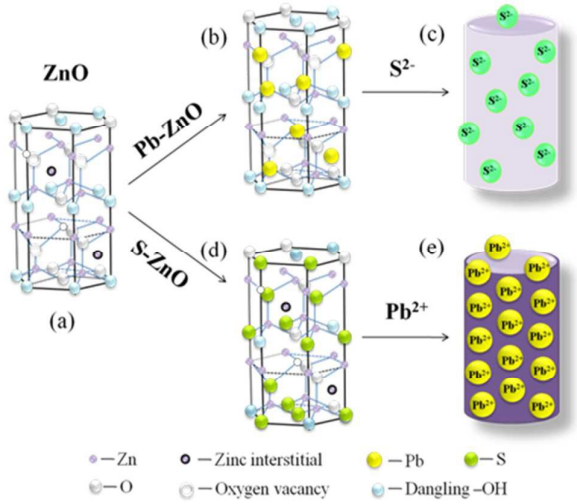

Figure 6 Schematic diagrams for the formation of PbS QDs on ZnO: (a) Schematic diagram for pure ZnO. (b) and (c) Schematic diagrams for formation of Pb-S-ZnO. (d) and (e) Schematic diagrams for formation of S-Pb-ZnO.

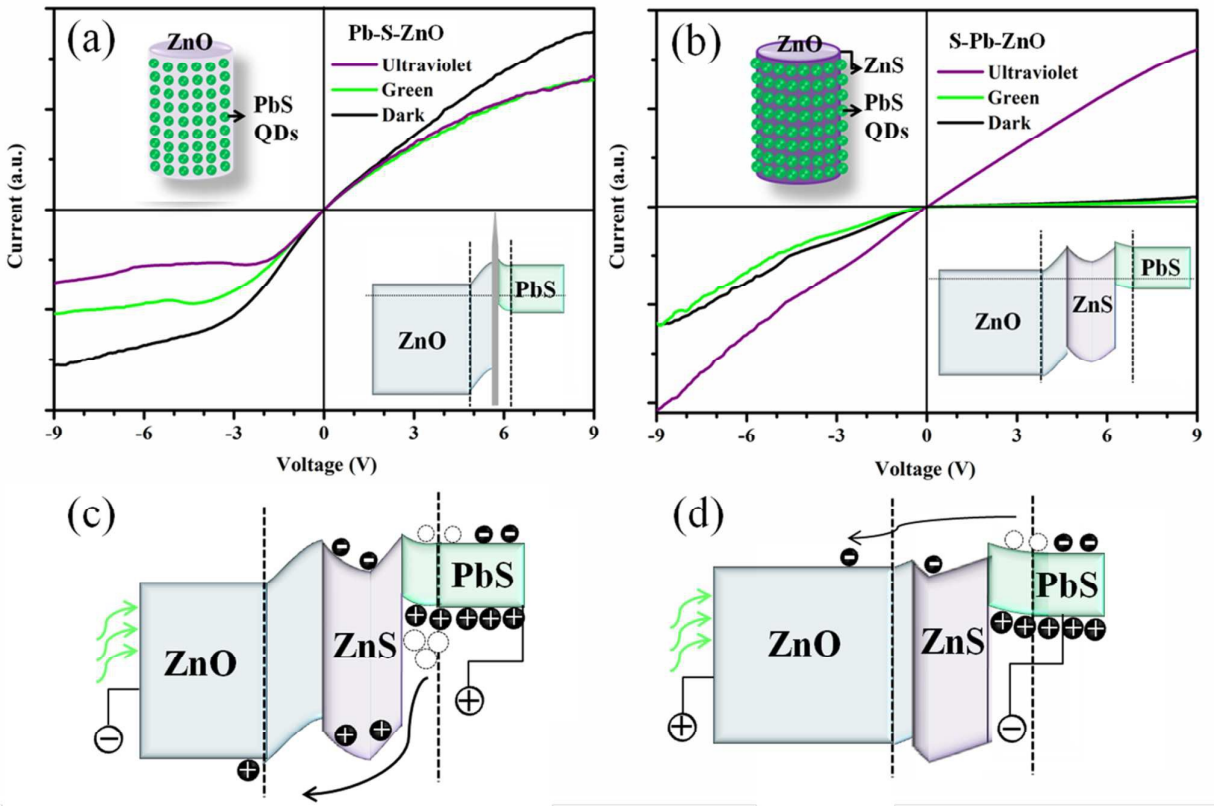

Figure 7 (a) and (b) I-V curves of Pb-S-ZnO and S-Pb-ZnO based heterostructures. Insets are the corresponding equilibrium schematic diagrams of the as-synthesized heterostructures and band structure diagrams at zero bias voltage. (c) and (d) Band structure diagrams of S-Pb-ZnO at different bias voltages under green light illumination.

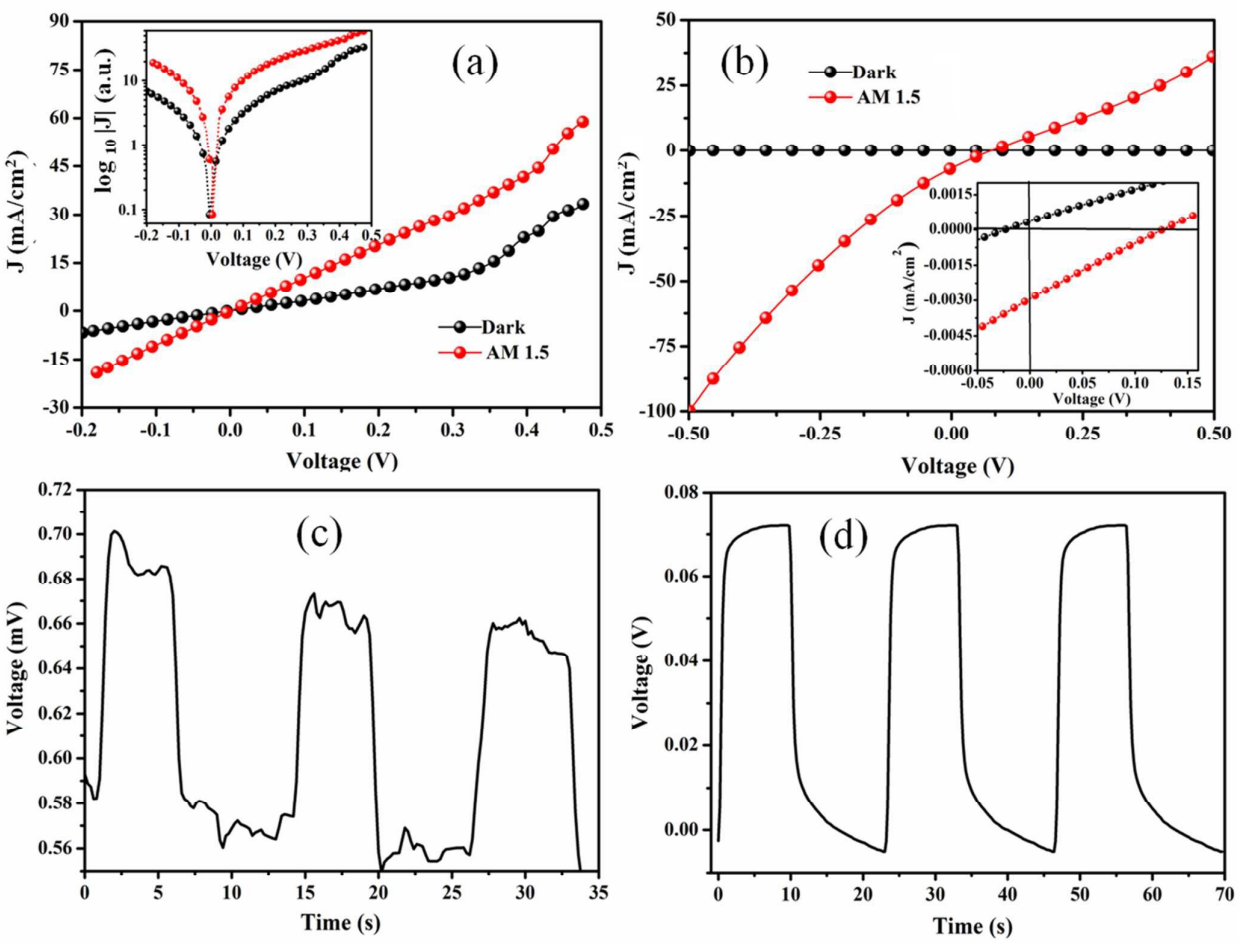

Figure 8 (a), (b) J-V curve of open solar cells formed by using Pb-S-ZnO and S-Pb-ZnO as anodes. (c) and (d) Time-dependent voltage response of Pb-S-ZnO and S-Pb-ZnO based solar cells. Inset in Figure 8 (a) is the J-V curve of Pb-S-ZnO based solar cell plotted with logarithmic scale for the y axis. Inset in Figure 8(b) is the enlarged J-V curve of S-Pb-ZnO based solar cell.